Mouse lung Tissue Resident Memory (TRM) CD8 T cell subsets have distinct metabolic profiles from each other and from non-TRM

Mike Sportiello[1,2], Alexis Poindexter[1], Emma C. Reilly[1], Adam Geber[1,2], Kris Lambert Emo[1], Taylor N. Jones[1], David J. Topham[1]

[1]Center for Vaccine Biology and Immunology, University of Rochester Medical Center, Rochester, NY, United States

[2] Medical Scientist Training Program, University of Rochester Medical Center, Rochester, NY 14642, USA

*** Correspondence:**

David J. Topham, PhD

David_Topham@urmc.rochester.edu

Abstract

Tissue resident memory CD8 T cells (T_{RM}) principally reside in peripheral non-lymphoid tissues and confer protection against a variety of illnesses ranging from infections to cancers. The functions of different CD8 T cell subsets in the skin have been linked with distinct metabolic pathways and differ from other CD8 T cell subsets. For example, they undergo fatty acid oxidation and oxidative phosphorylation to a greater degree than circulating memory and naïve cells. However, it is unclear if this programming is universal. Our work demonstrates T_{RM} are not homogenous and, based on integrin expression, exist as subsets with distinct gene expression and function. We hypothesize that lung T_{RM} with different integrin profiles will utilize unique metabolic programs. First, differential expression and pathway analysis was conducted on RNAseq datasets yielding important differences between subsets. Next, metabolic models were constructed and interrogated. Functional metabolite uptake assays were conducted, and the levels of oxidative phosphorylation, mitochondrial mass, and neutral lipids were measured. Furthermore, T cell differentiation studies were conducted varying concentrations of metabolites to investigate the causal relationship in T_{RM} development, demonstrating that, *in vitro*, lipid conditions impact memory cell maintenance generally, and that glucose concentration impacts T_{RM}-like differentiation specifically, with no effect on central memory-like T cell differentiation. In summary, a diverse set of analyses were utilized to demonstrate lung T_{RM} have unique metabolic profiles and that metabolic microenvironments alter differentiation *in vitro*.

1 Introduction

Tissue resident memory T cells (T_{RM}) confer protection against a variety of illnesses ranging from infectious diseases to cancers. As demonstrated in the skin, transfer of T_{RM} from immune to naïve hosts is sufficient to prevent herpes simplex virus type 1 (HSV-1)-associated pathology and, comparably, the presence of antigen-specific T_{RM} in a mouse model of melanoma can limit tumor growth (1, 2). In the lungs, T_{RM} are critical for protection against influenza and respiratory syncytial

38 virus, even in the absence of antibodies specific for those viruses (3, 4). T_{RM} have been shown to act
39 as both antigen-specific sentinels linking the innate and adaptive immune systems as well as cytotoxic
40 mediators themselves (5). This functional capacity makes them important players in immunity across
41 multiple organ systems and disease states.

42 TRM are heterogenous in terms of integrin expression, migration, effector potential, and gene
43 expression (5). Furthermore, the functions of different CD8 T cell subsets have been linked with
44 distinct metabolic pathways. For example, skin T_{RM} display a unique metabolic profile relative to other
45 CD8 memory cells subsets. They undergo fatty acid oxidation to a greater degree than other
46 circulating memory cells and naïve cells which tend to have higher glycolytic fluxes (6, 7). However, it
47 is unclear if this programming is universal among all T_{RM} subsets and whether it holds true in other
48 tissues such as the lung. It is also not yet know whether memory CD8 T cell subsets that express
49 different combinations of surface integrins CD49a and CD103 in addition to S1PR1 antagonist CD69
50 share metabolic profiles. Performing RNAseq on these populations yielded distinct transcriptomes (5),
51 suggesting the overall metabolic profiles may differ, perhaps to assist in their survival and function.
52 Furthermore, these unique integrin expression profiles could be linked to different tissue localization
53 and may require differential metabolic cell programming.

54 ## 2 Materials and Methods

55 ### *2.1 RNA sequencing analysis*

56 RNA sequencing data and lists of differentially expressed genes were obtained from previously
57 published work from our lab (GSE179653). Full code that generated those differentially expressed
58 genes as well as further analyses and figures is publicly available at https://github.com/sportiellomike.

59 ### *2.2 Metabolic modelling*

60 Mouse metabolic model iMM1865 was used as a starting point, onto which our publicly accessible
61 transcriptomic data for CD49a^{pos}CD103^{pos} (Double Positive, DP), CD49a^{pos}CD103^{neg} (CD49a Single
62 Positive, CD49a SP), or CD49a^{neg}CD103^{neg} (Double Negative, DN) was applied using the Gene
63 Inactivity Moderated by Metabolism and Expression (GIMME algorithm) (8). A threshold value of the
64 median transcript per kilobase million (TPM) for the 1,865 genes in the metabolic model was used.
65 Reaction constraints were added according to previously published research (9). All code used to
66 generate input data, figures, and the models themselves is available at
67 https://github.com/sportiellomike.

68 ### *2.3 Mice*

69 Mice were housed in approved microisolator cages, within a pathogen-free facility that is accredited
70 by the Association for Assessment and Accreditation of Laboratory Animal Care. It is staffed with a
71 number of personnel including those with expertise in husbandry, technical skills, and veterinary
72 personnel. C57BL/6J mice (Jackson Laboratories) used for experiments were infected 8-10 weeks
73 after birth. This study was carried out in strict accordance with the recommendations in the *Guide for*
74 *the Care and Use of Laboratory Animals* as defined by the NIH. The Institutional Animal Care and Use
75 Committee of the University of Rochester approved all protocols.

76 ### *2.4 Virus and infection*

77 Mice were anesthetized with 3,3,3-tribromoethanol. Upon verification of sedation, mice were infected
78 intranasally with 10^5 EID_{50} of HKx31 human influenza A virus in 30uL volume. After observation to
79 ensure they recovered from anesthesia, mice were monitored daily for weight and overall morbidity to
80 comply with all regulations.

81 ***2.5 Lung and Bronchoalveolar lavage processing***

82 Bronchoalveolar lavage (BAL) was collected by inserting a flexible Teflon catheter into a slit in the
83 trachea in proximity to the larynx. A 1mL syringe was connected to the catheter and the lungs were
84 flushed 3 times with 1x PBS (volumes of 1mL, 900uL, and 800uL). BAL was spun down at 424xg for
85 10 minutes. Red blood cells were eliminated through ACK mediated lysis. Cells were washed in 1x
86 PBS containing 1% FBS (PBS+serum) and resuspended in PBS+serum.

87 The lungs were harvested and separated into right and left lobes prior to collection into RPMI + 8%
88 FBS (Corning #10040CV). Lungs were transferred into Miltenyi Gentle MACS tubes containing 2 mL
89 of 2mg/mL collagenase II (Worthington #LS004177) and mechanically ground up by a Gentle MACS
90 machine. 3 additional mL of 2 mg/mL collagenase II solution was added before incubation for 30 min
91 at 37° C. Further mechanical digestion by Gentle MACS was done at this point. Tubes were spun at
92 233xg at room temperature for 2 minutes.

93 Pellets were then dissolved in existing supernatant and transferred through 100 μm strainers.
94 Contents were quantitatively transferred using 5 mL of RPMI + 8% FBS. Tubes were spun at 424xg
95 for 6 minutes at room temperature. The supernatant was discarded, and dissolved in 4 mL 40% Percoll
96 solution, which was then layered on 3 mL 75% Percoll solution. These tubes were then spun at 931xg
97 for 20 minutes at room temperature with no centrifuge break so as not to disturb the layers of the
98 gradient.

99 The top layer of lipid-rich liquid was aspirated off, and the interface (approximately 2 mL) of the two
100 Percoll densities was collected where the cells were. Tubes were filled with RPMI + 8% FBS and spun
101 down at 424xg for 6 minutes at room temperature.

102 ### *2.6 Spleen processing to achieve single cell suspension*

103 C57BL/6J mouse spleens were obtained from sacrificed mice and mechanically digested by grinding
104 between two frosted microscope slides without exogenous enzyme added. After grinding, Single
105 cell suspensions were passed through plastic mesh to capture large non-single cellular material and
106 centrifuged in conical vials at 424xg at 4°C for 6 minutes. Cells were resuspended in 3 mL of ACK
107 lysis buffer (Cold Spring Harbor Protocol: doi:10.1101/pdb.rec083295) for 5 minutes at room
108 temperature. Volume was brought up to 15 mL in PBS + serum followed by centrifuging at 424xg at
109 4°C for 6 minutes.

110 ### *2.7 T_{RM}-like Media preparation*

111 The following were added to 500 mL DMEM (Corning Catalog No. 10-017-CV): 50 mL fetal bovine
112 serum, 5 mL L-glutamine (Fisher Scientific Catalog No. 25030081), 12.5 mL HEPES buffer (Fisher
113 Scientific Catalog No. 15630080), 6.5 MEM Non-Essential Amino Acids Solution (Fisher Scientific
114 11140050), 0.6 mL of 1:300 dilution of beta mercaptoethanol in PBS, 5 mL penicillin streptomycin
115 (Fisher Scientific Catalog No. 15140122), 0.6 mL gentamycin (Fisher Scientific Catalog No.
116 15710064). Contents were sterile filtered.

117 ### *2.8 Fatty Acid Uptake*

118 Fatty Acid Uptake Media (FUM) was created by dissolving 2 µL stock solution made according to
119 package insert per 1 mL of Assay Buffer (AAT Bioquest Screen Quest Fluorimetric Fatty Acid Uptake
120 Assay Kit #36385). Once a single cell suspension was obtained from the harvesting protocol, cells
121 were plated in 100 µL of FUM and 100 µL Leibowitz media for a final volume of 200 µL. Vehicle control
122 used equivalent volume of dimethyl sulfoxide (DMSO) in Assay Buffer. Cells were incubated for 30
123 minutes at 37° C, then washed 1.5 times with PBS + 1% serum before staining.

124 ### *2.9 Neutral Lipid Staining*

125 Bodipy 505/515 (Fisher Scientific Catalog No. D3921) was dissolved in DMSO to yield a stock of 1
126 mg/μL concentration. Once a single cell suspension was obtained from the harvesting protocol, each
127 sample of cells in 1 mL of PBS were inoculated with Bodipy to yield a final concentration of 2 mg/mL,
128 or DMSO for the vehicle control. Samples were incubated for 30 minutes at 37° C, then washed 1.5
129 times with PBS + 1% serum before staining.

130 ***2.10 2-(N-(7-Nitrobenz-2-oxa-1,3-diazol-4-yl)Amino)-2-Deoxyglucose Uptake***

131 2-(N-(7-Nitrobenz-2-oxa-1,3-diazol-4-yl)Amino)-2-Deoxyglucose (2-NBDG) (Abcam Catalog No.
132 ab146200) was dissolved in DMSO to yield a 20 mM stock solution. After a single cell suspension was
133 obtained from the harvesting protocol, cells were resuspended in 500 μL non-supplemented Leibowitz
134 media and incubated at 37° C with a final 2-NBDG concentration of 80 μM or DMSO for the vehicle
135 control for 35 minutes at 37° C. Samples were washed 1.5 times with PBS + 1% serum before staining.

136 ***2.11 Mitochondrial Mass Quantification***

137 Mitotracker Green FM (Mitotracker) (Fisher Scientific Catalog No. M7514) was dissolved in DMSO to
138 obtain a 1 mM stock solution. After a single cell suspension was obtained from the harvesting protocol,
139 each sample was dissolved in 500 μL PBS + 1% serum. Samples were inoculated with Mitotracker
140 for a final concentration of 50 nM or equivalent volume of DMSO for the vehicle control and incubated
141 for 45 minutes at 37° C.

142 ***2.12 Oxidative Phosphorylation Quantification***

143 Tetramethylrhodamine, Ethyl Ester, Perchlorate (TMRE) (Cayman Chemical Catalog No. 701310)
144 was prepared in a 0.5 mM working stock by dissolving in DMSO, according to package insert. After a
145 single cell suspension was obtained from the harvesting protocol, TMRE was added to two separate
146 aliquots of 5 mL RPMI + 8% FBS (TMRE Media) for a final concentration of 250 nM. To one of these
147 aliquots, 2-[2-[4-(trifluoromethoxy)phenyl]hydrazinylidene]-propanedinitrile (FCCP) was added
148 (FCCP-TMRE Media) for a final concentration of 1 μM. Samples were split into two and dissolved into

149 500 µL of either TMRE Media or FCCP-TMRE Media. Samples were incubated at 37° C for 30
150 minutes. For vehicle control, DMSO was added in place of TMRE. Cells were washed 1.5 times with
151 PBS + 1% FBS prior to staining.

152 **2.13 T_{RM}-like cell culture conditions**

153 24 well plates were coated with anti-CD3/28 stimulating antibodies (Biolegend Catalog Nos. 100302
154 and 102102) at final concentration of 5 µg/mL each overnight at 4° C. The next day, 2 million single
155 cell splenocytes were plated in 1 mL T_{RM}-like culture media onto each well with 7.5 ng/mL human IL-
156 2 (Obtained from the NIH). Two days later, cells were collected, centrifuged at 424xg at 4° C for 6
157 minutes, and plated onto non-coated 24 well plates in 1 mL TRM-like culture media with 7.5 ng/mL
158 IL-2 for three days. After that, cells were collected, centrifuged at 424xg at 4° C for 6 minutes, and
159 plated in TRM-like culture media with 10 ng/mL mouse IL-7 (Biolegend Catalog No. 577804) and 10
160 ng/mL human TGFβ1 (Fisher Scientific PHG9214) for 6 days.

161 Additional glucose (Fisher Scientific Catalog No. A2494001) and lipid supplement (Millipore Sigma
162 Catalog No. L5146) were added to TRM-like cell culture media starting from the day of spleen
163 harvest (day 0) throughout the end of the experiment (day 11, day 6 post TGFβ1 addition). Soluble
164 lipid stores were created in Kolliphor P 188 (Millipore Sigma K4894) according to lipid supplement
165 instructions.

166 ***2.14 Staining for Flow Cytometry***

167 Cells were suspended in 100 µL staining buffer for 30 minutes at 4° C. Staining buffer was created by
168 adding staining antibodies to PBS below for a final concentration of 1 µg/mL each, or 0.2 µL of live-
169 dead stock solution/100 µL staining buffer. Live-dead stock solution was prepared according to
170 package insert available on the vendor website. αCD16/32 was added for a final concentration of 2.5
171 µg/mL. αCD45 was previously injected at time of organ harvest intravenously at a concentration of 0.2
172 µg stock antibody/100 µL PBS in a volume of 100 µL. See table S1 for more information. All antibodies
173 used Bangs Laboratories compensation beads (Bangs #556) which were stained an equivalent time.

174 Live-dead stain used Life Technologies ArC reactive beads (Invitrogen A10346). Because the vast
175 majority of cells at day 14 post infection will have been antigen experienced, CD44 was not used as
176 a marker on day 14 experiments. Experiments were run on an 18-color BD LSR II flow cytometer.
177 Gating strategy is displayed in Figure S1.

178 ***2.15 MFI Determination and Normalization***

179 The four subsets of interest were manually gated after selecting for lymphocytes (FSC-A and SSC-
180 A), singlets (FSC-A and FSC-H), live cells, IV-CD45^{neg} cells, TCRβ^{high} and CD8α^{high} cells. DN (Double
181 Negative) was defined as CD103^{low} and CD49a^{low}, DP (Double Positive) as CD103^{high} and CD49a^{high},
182 CD103 SP (CD103 Single Positive) as CD103^{high} CD49a^{low}, and CD49a SP (CD49a Single Positive)
183 as CD49a^{high} and CD103^{low}.

184 Median fluorescence intensities (MFIs) were calculated using Flowjo (version 10.6.2). Data was
185 normalized by dividing the MFI of each subset by the sum of all four subsets' MFIs for each mouse
186 and multiplying by 4. For the assays using TMRE, FCCP was subtracted from the TMRE MFI for each
187 subset within each mouse. That number was divided by the sum of MFIs of the uncoupled control
188 (FCCP+TMRE) subsets for each mouse. Normalized data can be found at
189 https://github.com/sportiellomike.

190 ***2.16 Statistical Tests***

191 After repeated measures ANOVA, Multiple pairwise comparisons were evaluated using the Student's
192 T test with Benjamini-Hochberg correction. If $P_{adjusted}<0.05$, results were deemed significant. For the
193 linear regression analysis, Pearson's method was used. R Packages ggplot2 (version 3.3.2) and
194 rstatix (0.7.0) were used for data plotting and statistical testing respectively. The code used to perform
195 statistical tests and generate figures can be found here: https://github.com/sportiellomike.

196 **3 Results**

197 ***3.1 Pathway analysis for metabolic analyses.***

198 T_{RM} can be defined by their surface protein expression and multiple markers have been used to
199 including CD69, CD49a, and CD103. In the lung, CD44 expression identifies antigen-experienced
200 memory T cells while CD49a^{pos} marks T_{RM}, and when used in combination with CD103, yields two T_{RM}
201 subsets: CD49a^{pos}CD103^{pos} (Double Positive, DP) and CD49a^{pos}CD103^{neg} (CD49a Single Positive,
202 CD49a SP) (5). At later memory time points, very few CD49a^{neg}CD103^{pos} (CD103 Single Positive,
203 CD103 SP) remain, suggesting they have either died, left the tissue, or altered their integrin
204 expression. CD49a^{neg}CD103^{neg} cells that remain at this time point resemble T cells with an Effector
205 Memory phenotype (T_{EM}) and may be circulating (5). To more fully describe the metabolic profiles of
206 T_{RM} based on integrin expression, we utilized the publicly accessible RNA sequencing data set we
207 previously reported (5). This data set was generated from antigen-experienced mouse lung tissue
208 CD8 T cells 21 days post infection (dpi) that were sorted by CD49a and CD103 expression and
209 submitted for poly-A enriched mRNA sequencing. Double Negative cells (DN) were defined as
210 CD103^{neg} and CD49a^{neg}, Double Positive (DP) as CD103^{pos} and CD49a^{pos}, CD103 Single Positive
211 (CD103 SP) as CD103^{pos} CD49a^{neg}, and CD49a Single Positive (CD49a SP) as CD49a^{pos} and
212 CD103^{neg}.

213 Using P_{adj} <0.05 as a cutoff, the data were analyzed using Log_2(Fold Change) (LFC) cutoffs of >0.5
214 or <-0.5 to determine up- or downregulated genes, respectively. Per pathway analysis, there were no
215 enriched pathways in either the up- or downregulated genes when comparing DP to CD49a SP. Seven
216 pathways from the Reactome database were upregulated in DP vs DN, including *Metabolism of lipids*
217 *and lipoproteins*, *Fatty acid, triacylglycerol, and ketone body metabolism*, and *Cholesterol*
218 *biosynthesis* (**Figure 1A**), with a large number of downregulated pathways, largely related to RNA
219 translation and decay. Equivalent analysis using the KEGG database yielded eight upregulated
220 pathways including *Steroid biosynthesis*, with just one downregulated pathway *Ribosome* (**Figure**
221 **1B**). Many pathways including *Fatty acid biosynthesis*, *Fatty acid degradation*, and *Fatty acid*
222 *elongation* were not significantly different in the pathway analysis using KEGG.

223 Interestingly, CD49a SP, though indistinguishable from DP at the global transcriptomic level (5), did
224 not share any strictly metabolic pathways from Reactome with DP (**Figure 1C**). They also did not
225 share any with each other in the KEGG database beyond *Steroid biosynthesis* (**Figure 1D**).
226 Specifically, CD49a SP did not share *Cholesterol biosynthesis*, *Regulation of cholesterol biosynthesis*
227 *by SREBP (SREBF)*, *Metabolism of lipids and lipoproteins*, or *Fatty acid, triacylglycerol, and ketone*
228 *body metabolism* which were all upregulated in DP vs DN but not CD49a SP vs DN. Metabolic
229 differences between DP and DN but not CD49a SP and DN could imply metabolic differences between
230 CD49a SP and DP that these pathway analysis methods are not sensitive enough to distinguish.

231 **3.2 *Metabolic modelling predicts lipid-centric metabolism in T_{RM}***

232 Having performed basic pathway analyses and discovering a possible enrichment for lipid-centric
233 programming in T_{RM}, we were interested in modelling the metabolome of lung CD8 T cells using the
234 entirety of the transcriptomic data to see if this more intensive approach yielded similar results.

235 Therefore, three metabolic computational models were constructed: one for lung CD8 T cells
236 expressing both CD49a and CD103 (*tissuemodelDP*), one for the single positive subset
237 (*tissuemodelCD49aSP*) and one for the subset expressing neither integrin (*tissuemodelDN*).
238 Because so few CD103 SP cells exist at memory timepoints, a metabolic model was not created for
239 this subset. These novel models together represent nearly all antigen experienced CD8 T cells in
240 mouse lung, encompassing both T_{RM} and non-T_{RM} cells that happen to be trafficking through the
241 lung.

242 Briefly, the published mouse metabolic model iMM1865 was used as a starting point (10). Then, the
243 Gene Inactivity Moderated by Metabolism and Expression (GIMME) algorithm was implemented in
244 COBRA Toolbox (11) to conduct a flux balance analysis using our RNAseq transcript level data to
245 inform the level of flux for each reaction (8). When building metabolic models, an objective function
246 must be selected for which flux is to be maximized given the constraints. In line with the majority of
247 other metabolic models, “BIOMASS” was selected, which itself is a combination of a number of

248 reactions related to cell maintenance that must have positive flux for cells to be viable. Given our
249 constraints, a single, nonzero optimal solution was predicted for all three of our models.

250 Our model predicted that our DP subset had the greatest flux through its Beta Oxidation of Fatty
251 Acids pathway, consistent with our initial pathway analysis (Figure 2). In addition, our CD49aSP
252 subset differed from our DP subset with less flux through that pathway than both DP and DN, again
253 consistent with initial pathway analysis. These results, in addition to our initial pathway analysis,
254 imply differences in T_{RM} metabolism between DP and CD49a SP subsets.

255 *3.3 Tissue resident memory CD8 T cell subsets have unique metabolic profiles directly ex*
256 *vivo*

257 Thus far, our transcriptomic analyses were largely consistent with that demonstrated for T_{RM} in skin.
258 Nonetheless, transcriptomic data and metabolic modelling do not clearly demonstrate that functional
259 differences exist between T_{RM} subsets or between circulating cells and T_{RM}. To further understand
260 these T_{RM}, a Seahorse XF Mito Fuel Flex Test assay was performed. However, even after pooling the
261 T cells subsetted from 40 mice, the signal was not high and reproducible enough to draw conclusions
262 (data not shown), suggesting this approach is not feasible in this context. Instead a flow-cytometric
263 approach was performed. To determine if the T_{RM} subsets display any differences in their
264 mitochondria, the mitochondrial mass of cells of different integrin profiles at 14 days post infection
265 (dpi) were evaluated by Mitotracker Green FM (Mitotracker) staining. Mitotracker preferentially
266 accumulates in mitochondria by covalently binding free thiol groups independent of mitochondrial
267 membrane potential (12). Mice were infected with HKx31 influenza virus and cells were collected at
268 14 dpi, a time when CD8 T cells with a T_{RM} phenotype are numerous. Both airway cells harvested
269 through bronchoalveolar lavage (BAL) and cells remaining in the tissue after lavage (likely lung
270 parenchymal cells) were examined for Mitotracker staining. To ensure that cells in the lung tissue
271 were not associated with or within the vasculature, a standard intravenous (IV) labeling exclusion
272 approach was utilized (5).

273 We found that both DP and CD103 SP contain higher mitochondrial mass than the DN subset (**Figure**
274 **3A**). Similar results were found in BAL, though the comparison between CD103 SP and DN did not
275 achieve significance (**Figure S2**). Mitochondrial mass was also assessed at 62 dpi. CD103 SP cells
276 were not included in this analysis because so few cells could be detected. At this later timepoint,
277 CD49a SP had significantly lower levels of mitochondrial mass than its DP and DN counterparts in
278 the lung (**Figure 3B**). Day 62 may be considered by some to be a more classical "memory" time point,
279 suggesting mitochondrial mass changes in some subsets as memory develops.

280 The question of whether the cell populations displayed differential mitochondrial functions, not just
281 different mitochondrial masses, remained. Oxidative phosphorylation is a primary role of the
282 mitochondrion, as it is the most efficient means by which a cell can generate ATP. Cells with equivalent
283 mitochondrial mass could potentially undergo differential rates of oxidative phosphorylation and
284 therefore ATP production. To evaluate this level of oxidative phosphorylation, TMRE, a fluorescent
285 dye preferentially taken up by active mitochondria with membrane potentials, was used. To remove
286 background staining, an equivalent sample was treated with both TMRE and the decoupling agent
287 FCCP, whose MFI was subtracted from the treatment group's MFI.

288 Cells in the lung expressing CD103 (DP and CD103 SP) had increased TMRE staining implying a
289 greater degree of oxidative phosphorylation (**Figure 3C**). Later, at 62 dpi, no comparison was
290 significantly different (**Figure 3D**). At 62 dpi, DP and DN cells have more mitochondrial mass than the
291 CD49 SP subset (**Figure 3B**), while undergoing the same amount of oxidative phosphorylation
292 (**Figure 3D**). This implies that at later memory timepoints, DP and DN cells have a higher spare
293 respiratory capacity (SRC): they may have the capability to use their higher amounts of mitochondria
294 to produce more ATP after reactivation. This is a well-documented phenomenon when comparing
295 memory T cells to effector T cells or naïve T cells, but never before have different T_{RM} subsets been
296 compared this to each other (13). Generally, memory cells have a higher SRC than effector cells. This
297 increased spare respiratory capacity in DP but not CD49a SP could imply different roles in memory
298 and effector responses in the lung post infection.

299 Based on the observed differences, we wanted to investigate whether nutrient uptake was altered in
300 a similar way. Glucose is a metabolically essential molecule in a variety of cellular processes as both
301 an eventual source of cell energy in the form of ATP as well as a carbon source in anabolism. To
302 evaluate the extent to which glucose was being taken up by the CD8 T cells, we utilized the glucose
303 analogue 2-NBDG. This fluorescent analogue undergoes facilitated diffusion through glucose
304 transporters GLUT1-4 as well as through active transport through SGLT1 and 2, recapitulating the
305 kinetics of glucose transport (14-19). It is phosphorylated by hexokinase after entering the cell, which
306 traps the fluorescent molecule in the cell, but cannot proceed further in glycolysis.

307 DP and CD49a SP displayed similar levels of glucose uptake 14 dpi, however, these populations
308 displayed lower levels of 2-NBDG staining compared with DN and CD103 SP cells, suggesting that
309 CD49a expressing subsets may be less glucose-dependent than CD49a negative counterparts
310 (**Figure 3E**). A similar pattern was observed in BAL samples, with CD49a^{pos} subsets taking up lower
311 levels of the dye. This pattern was conserved through later memory timepoints 60+ dpi (**Figure 3F**)
312 and are consistent with studies done on T_{RM} in the skin, which noted an increased dependence on
313 free fatty acids (FFAs) as opposed to glucose (7) in T_{RM}.

314 Based on these findings, we hypothesized that lung T_{RM} utilize a more lipid-centric metabolism. This
315 was originally hypothesized in skin due to its lipid-rich environment, though the lung is significantly
316 less lipid-rich (7). Having demonstrated significant differences in glucose uptake, we next investigated
317 the ability of T cells to take up free fatty acids. A fluorescently conjugated fatty acid (FFA) was utilized.
318 In the lung parenchyma, CD49a^{pos} subsets (CD49a SP and DP) took up the highest amount of FFA.
319 (**Figure 3G**). Similar results were found in BAL. These findings were similar but importantly distinct at
320 60+ dpi: DP took up more FFAs than CD49a SP which in turn took up equivalent FFAs as DN (**Figure**
321 **3H**). Other studies that have reported a dependence of T_{RM} on FFAs have never used CD49a as a
322 marker (7). We expected our results to demonstrate that both DP and CD49a SP (the latter not studied
323 by other metabolic studies) were dependent on these FFAs in the lung, but we found this only to be
324 true at 14 dpi. At 60+ dpi, The CD49a SP were much more similar to DN, indicating an important

325 functional difference. From this data, we hypothesize that CD49a SP utilizes a less lipid centric
326 metabolic strategy to maintain residency than their DP counterparts.

327 We next wanted to determine if there were further differences in lipid metabolism. To address this,
328 Bodipy, a molecule that is taken up passively and stains cellular stores of neutral lipids, was used to
329 quantify the amount of neutral lipids present in lung T cells (20). Neutral lipids serve as a store of
330 potential energy as well as a carbon source, a valuable resource if the cells were to expand and
331 undergo effector functions in a nutrient deficient environment.

332 Nearly identical patterns for BAL and lung were observed 14 dpi (**Figure 3I, J, Figure S2**). DP cells
333 displayed the highest levels of neutral lipid storage, followed by CD49a SP, DN, with the lowest levels
334 in CD103 SP. While all six comparisons demonstrate that the four subsets are significantly different
335 from one another, it is remarkable that the subsets expressing CD49a (CD49a SP and DP) stain
336 brightly for neutral lipids while those not expressing CD49a (CD103 SP and DN) display low levels.
337 Having quick access to neutral lipids for both energy and carbon needs may prove important for their
338 function. Interestingly, the differences observed at 14 dpi were not seen at 60+ dpi.

339 ***3.4 Glucose-rich metabolic microenvironments alter differentiation of T_{RM}-like cells in vitro***

340 Noting the myriad of differences between T_{RM} and non-T_{RM}, as well as among T_{RM} subsets, we
341 hypothesized that these effects may not only be phenotypic differences among these CD8 T cell
342 subsets, but that the metabolic microenvironment is deterministic in their differentiation. To test this,
343 T_{RM}-like T cells were generated *in vitro* so that that the metabolic microenvironment could be closely
344 controlled. T_{RM}-like cells can be generated *in vitro* stimulating naïve mouse splenocytes on anti-
345 CD3/CD28 coated plates for two days in the presence of IL-2 followed by three days in non-coated
346 plates supplemented with IL-2, and finally in IL-7 and TGF-β for six days to illicit a T_{RM}-like
347 phenotype, as previously described (21). Both the concentration of glucose as well as lipids were
348 varied (**Figure 4**) to test the effects given levels of glucose or lipids have as well as across levels.

349 First, the effect of glucose was examined within each lipid concentration, ranging from 0x to 8x
350 recommended supplementation (Millipore Sigma #L5146). Without exogenous lipid added, there
351 was no effect of glucose concentration on frequency, but with 2x or 4x lipid supplementation,
352 generally, as the concentration of glucose increased, the cell number normalized per volume and
353 frequency of CD49a positive cells both decreased (**Figures 5A and 5B**). The number of live CD8 T
354 cells for the 8x lipid supplementation group was effectively zero by this timepoint, and for the other
355 three groups the linear relationship between absolute number of CD49a positive cells per volume
356 and glucose concentration was significant for the 0x, 2x, and 4x lipid supplementation groups
357 (*P*=2.9e-6, 1.4e-9, 8.2e-6, R=-0.66, -0.79, and -0.64 respectively) (**Figure 6A**). In line with that
358 finding, the relationship between the frequency of CD49a positive cells and glucose concentration
359 was significant for both the 2x and 4x lipid supplementation groups (*P*=4.5e-13 and 1.3e-4, R= -0.87
360 and -0.57 respectively) (**Figure 6B**). Overall, this paints a picture of increasing glucose
361 concentration causing a decrease in both the frequency and absolute number of CD49a positive
362 cells. This is in contrast to the frequency of central memory marker CCR7 positivity (**Figures 6C and**
363 **6D, 7A-7D**), which was not significant for any lipid supplementation concentration, though increasing
364 concentrations of glucose did seem to decrease the number of CCR7 positive cells per microliter at
365 lipid concentrations 0x, 2x, and 4x.

366 When analyzing the effect of lipid on the differentiation of CD8 T cells *in vitro*, a contrasting pattern
367 emerged: within each concentration of glucose, increasing lipid concentration from 0x to 2x
368 increased the frequency of CD49a positive cells at the lowest and second lowest concentrations of
369 glucose tested (4.5 and 9.5 mg/mL) (**Figure 5C**), but further addition of lipid to 4x did not increase
370 the frequency of CD49a positive cells. The absolute number of CD49a positive cells per volume
371 peaked at 2x and decreased upon further addition of lipid for all concentrations of glucose tested. A
372 similar finding occurred for CCR7 positivity (**Figure 5D**).

373 Taken together, these results imply that high glucose concentration was detrimental to the long-term
374 viability or maintenance of CD8 T cells independent of lipid supplementation, and affects the

375 differentiation of CD49a positive cells, not CCR7 positive cells, at least in this assay. Furthermore,
376 lipid supplementation is beneficial up to a point, and then may become toxic as measured by the
377 number of live CD8 T cells in culture. It is beneficial for both CD49a and CCR7 positivity.

378 **4 Discussion**

379 We found memory T cell subsets in the lung exhibit distinct metabolic profiles. Furthermore,
380 experiments conducted to differentiate T_{RM} in the presence of varying metabolic substrates suggest
381 metabolite availability can influence memory T cell differentiation and survival. This availability may
382 be due local presence or lack of presence, the cell's ability to transport said metabolite into the cell,
383 or expression of receptor(s) to interact with these metabolites from outside the cell.

384 Differential expression, pathway, and metabolic modeling analyses of our RNAseq experiment led to
385 the hypotheses that lung T_{RM} have distinct metabolic programming compared with circulating cells.
386 Using both functional and descriptive methods, we produced a dataset for a variety of cell functions
387 including mitochondrial profiling, nutrient uptake, and more at both 14 and 60+ dpi. Synthesizing these
388 data together, what seems clear is that DP and CD49a SP, though different from each other in a few
389 assays, share a similar pattern. This pattern is distinct from DN, the subset presumably consisting of
390 T cells mostly with the phenotypes of effector memory and some central memory (5). DP and CD49a
391 SP both take up more fatty acids, store more neutral lipids, and take up less glucose than DN cells at
392 14 dpi. At later memory time points, DP and CD49a SP diverge: DP have more mitochondrial mass,
393 uptake less glucose, and uptake more fatty acid than CD49a SP. These changes from 14 to 60 dpi
394 could be a result from a change in the actual metabolic profile of these cells, a change in integrin
395 expression, cells dying, and/or cells leaving the tissue. These differences make the CD49a SP
396 population, well validated to be resident in the lung, an interesting subset of T_{RM} with respect to their
397 metabolism. These findings all correlate with a more "resting" memory phenotype for DP versus the
398 perhaps more "activated" CD49a SP. We have previously reported that the CD49a SP subset has a

399 number of features that correlate with a more effector-like phenotype such as having a higher
400 frequency of Granzyme B and perforin double positive cells, poised for cell killing (5).

401 The metabolic profile of an individual T cell as well as a T cell subset population are important
402 functionally, as we know many cell signaling molecules are limiting. Indeed, this is a leading
403 hypothesis as to why some T cells become T_{RM} and some do not (21). The functions of these subsets
404 during a subsequent infection may in part be achieved through the availability of different nutrients: if
405 T_{RM} depend mostly on uptake of free fatty acids whereas naive and effector T cells depend on glucose
406 uptake, both may be able to perform their functions more optimally with less competition for energy
407 resources existing between them. Furthermore, these profiles directly impact the cell signaling the
408 cells may be receiving. It is known that altering the ability for naïve CD8 T cells to take up glucose
409 directly impacts its future likelihood of becoming a memory cell (22). Having a metabolic profile that,
410 at baseline, is not dependent on glucose may ensure that the internal cell signaling conferring this
411 memory phenotype continues to do so in a positive feedback manner. Furthermore, upon infection,
412 the most glucose-starved T cells become memory cells (22). TCR stimulation is directly related to
413 specificity of binding and the abundance of a TCR's peptide:MHC complex. Others have shown that
414 T cells take up more glucose when more activated (23). Having an abundance of high-affinity
415 interactions with peptide:MHC complexes may cause a hyper local effect of glucose starvation. The
416 same group demonstrated that decreased availability of glucose led to increased memory CD8 T cell
417 populations. The fact that these T_{RM} and other memory cells seem to demonstrate lipid-centric
418 metabolism may assist naïve T cells to respond to infection because they don't compete with other
419 memory cells for glucose: if memory cells utilize one energy source (lipids), but naïve are more
420 dependent on another (glucose), it is less likely that memory T cells will starve out the naïve
421 responses, eliciting a more diverse group of memory T cells at the end of that infection, which would
422 increase the likelihood of a productive immune response upon a subsequent heterologous infection
423 since there is a more diverse and potentially cross-reactive set of T cells.

424 The causal effect of metabolic factors on CD8 T cell differentiation has been studied but never in the
425 context of T_{RM} differentiation. In short, we found glucose to be detrimental for the expression of T_{RM}
426 marker CD49a in a linear manner, whereas we found increasing lipid beneficial, to a point. Conversely,
427 glucose did not affect the expression of central memory marker CCR7, whereas the effect of lipids
428 was similar for both CD49a and CCR7: there exists an optimal concentration above and below which
429 decreases the expression of these markers. We believe these findings have direct implications for the
430 creation of therapies like CAR-T cells which necessitate *ex vivo* culture conditions: these conditions
431 should be optimized for the most efficacious T cell response which could include the optimization of
432 these culture conditions for the creation of T_{RM}, since tumor infiltrating lymphocytes have a T_{RM}-like
433 phenotype and are associated with positive outcomes (24-27). Future studies should assess this
434 possibility.

435 **5 Figure Legends**

436 **Figure 1. Significantly up and downregulated Reactome and KEGG pathways in mouse lung**
437 **memory CD8 T cells 21 days post infection**

438 (A) Reactome and KEGG databases were queried with the lists of differentially expressed genes
439 between DP and DN. (B) Reactome and KEGG databases were queried with the lists of differentially
440 expressed genes between CD49a SP and DN. Criteria for inclusion as differentially expressed genes
441 include $P_{adj} < 0.05$ and Log_2(Fold Change) > 0.5 or Log_2(Fold Change) < -0.5. DP. Adjusted P value
442 cutoff for enrichment is $P_{adj}<0.05$. (Double Positive, $CD49a^{pos}CD103^{pos}$); DN (Double Negative,
443 $CD49a^{neg}CD103^{neg}$); CD49a SP (CD49a Single Positive, $CD49a^{pos}CD103^{neg}$).

444 **Figure 2. Fatty acid oxidation net fluxes for DP, CD49a SP, and DN models.**

445 Metabolic models were created and beta oxidation of fatty acid net flux (mmols per gram dryweight
446 hours) levels were reported for each memory CD8 T cell subset. DP (Double Positive,

447 CD49a^{pos}CD103^{pos}); DN (Double Negative, CD49a^{neg}CD103^{neg}); CD49a SP (CD49a Single Positive,
448 CD49a^{pos}CD103^{neg}).

449 **Figure 3. Normalized mouse IV-label-negative lung CD44^{pos} CD8 T cell MFIs from flow**
450 **cytometric assays.**

451 Normalized MFIs plotted for each assay at 14 and 60+ days post infection. *P < 0.05, **P < 0.01, ***P
452 < 0.001, ****P < 0.0001. DP (Double Positive, CD49a^{pos}CD103^{pos}); DN (Double Negative,
453 CD49a^{neg}CD103^{neg}); CD49a SP (CD49a Single Positive, CD49a^{pos}CD103^{neg}) ; CD103 SP (CD103
454 Single Positive, CD49a^{neg}CD103^{pos}).

455 **Figure 4. Assay layout for T cell differentiation studies.**

456 16 combinations (4 glucose treatment groups, 4 lipid treatment groups permuted) were assayed.

457 **Figure 5. Metabolite concentration impact on T_{RM}-like cell differentation and maintenance *in***
458 ***vitro*.**

459 Percent CD49a positive (A and C) and cell number per µL (B and D) in metabolite alteration assays
460 where both lipid (0x-8x) and glucose (4.5-24.5 mg/mL) were altered. *P < 0.05, **P < 0.01, ***P <
461 0.001, ****P < 0.0001. Small circles represent individual data points.

462 **Figure 6. Simple linear regression modeling the effect of glucose concentration on CD49a and**
463 **CCR7 positivity.**

464 Simple linear regression of (A) CD49a positive cells per µL ~ glucose concentration, (B) percent
465 CD49a positive ~ glucose concentration, (C) CCR7 positive cells per µL ~ glucose concentration, and
466 (D) percent CCR7 positive ~ glucose concentration. Small circles represent individual data points.
467 Large circles represent the mean of those for each glucose cocentration. Background represents 95%
468 confidence interval of the best fit line.

469 **Figure 7. Metabolite concentration impact on T_{CM}-like cell differentation and maintenance *in*
470 *vitro*.**

471 Percent CCR7 positive (A and C) and cell number per µL (B and D) in metabolite alteration assays
472 where both lipid (0x-8x) and glucose (4.5-24.5 mg/mL) were altered. *P < 0.05, **P < 0.01, ***P <
473 0.001, ****P < 0.0001. Small circles represent individual data points.

474 **6 Author Contributions**

475 MS designed and performed experiments, analyzed and interpreted data, and wrote the manuscript.
476 AP assisted in conducting experiments and assay optimization. AG, KL, ECR, and TJ edited the
477 manuscript. ECR and KL provided technical support. DJT provided overall direction, procured
478 funding, interpreted data, and edited the manuscript.

479 **7 Acknowledgments**

480 We acknowledge the important contribution of the University of Rochester Medical Center Genomic
481 Research Center, Flow Core, and Vivarium staff. In addition, we are gracious and acknowledge the
482 supplying of reagents by Andrea Amitrano, PhD and Minsoo Kim, PhD.

483 **8 Data Availability Statement**

484 The datasets for this study can be found on GitHub (https://github.com/sportiellomike). Previously
485 published RNAseq data sets were used and are available here: Geo with accession GSE179653
486 (https://www.ncbi.nlm.nih.gov/geo/query/acc.cgi?acc=GSE179653).

487 **9 References**

488 1. Park SL, Buzzai A, Rautela J, Hor JL, Hochheiser K, Effern M, et al. Tissue-resident memory
489 CD8(+) T cells promote melanoma-immune equilibrium in skin. Nature. 2019;565(7739):366-71.

490 2. Park SL, Zaid A, Hor JL, Christo SN, Prier JE, Davies B, et al. Local proliferation maintains
491 a stable pool of tissue-resident memory T cells after antiviral recall responses. Nat Immunol.
492 2018;19(2):183-91.

493 3. Ray SJ, Franki SN, Pierce RH, Dimitrova S, Koteliansky V, Sprague AG, et al. The collagen
494 binding alpha1beta1 integrin VLA-1 regulates CD8 T cell-mediated immune protection against
495 heterologous influenza infection. Immunity. 2004;20(2):167-79.

496 4. Jozwik A, Habibi MS, Paras A, Zhu J, Guvenel A, Dhariwal J, et al. RSV-specific airway
497 resident memory CD8+ T cells and differential disease severity after experimental human infection.
498 Nat Commun. 2015;6:10224.

499 5. Reilly EC, Sportiello M, Emo KL, Amitrano AM, Jha R, Kumar ABR, et al. CD49a Identifies
500 Polyfunctional Memory CD8 T Cell Subsets that Persist in the Lungs After Influenza Infection. Front
501 Immunol. 2021;12:728669.

502 6. Pan Y, Kupper TS. Metabolic Reprogramming and Longevity of Tissue-Resident Memory T
503 Cells. Front Immunol. 2018;9:1347.

504 7. Pan Y, Tian T, Park CO, Lofftus SY, Mei S, Liu X, et al. Survival of tissue-resident memory
505 T cells requires exogenous lipid uptake and metabolism. Nature. 2017;543(7644):252-6.

506 8. Becker SA, Palsson BO. Context-specific metabolic networks are consistent with
507 experiments. PLoS Comput Biol. 2008;4(5):e1000082.

508 9. Han F, Li G, Dai S, Huang J. Genome-wide metabolic model to improve understanding of
509 CD4(+) T cell metabolism, immunometabolism and application in drug design. Mol Biosyst.
510 2016;12(2):431-43.

511 10. Khodaee S, Asgari Y, Totonchi M, Karimi-Jafari MH. iMM1865: A New Reconstruction of
512 Mouse Genome-Scale Metabolic Model. Sci Rep. 2020;10(1):6177.

513 11. Heirendt L, Arreckx S, Pfau T, Mendoza SN, Richelle A, Heinken A, et al. Creation and
514 analysis of biochemical constraint-based models using the COBRA Toolbox v.3.0. Nat Protoc.
515 2019;14(3):639-702.

516 12. Presley AD, Fuller KM, Arriaga EA. MitoTracker Green labeling of mitochondrial proteins
517 and their subsequent analysis by capillary electrophoresis with laser-induced fluorescence detection.
518 J Chromatogr B Analyt Technol Biomed Life Sci. 2003;793(1):141-50.

519 13. van der Windt Gerritje JW, Everts B, Chang C-H, Curtis Jonathan D, Freitas Tori C, Amiel E,
520 et al. Mitochondrial Respiratory Capacity Is a Critical Regulator of CD8+ T Cell Memory
521 Development. Immunity. 2012;36(1):68-78.

522 14. Lu Y-T, Ma X-L, Xu Y-H, Hu J, Wang F, Qin W-Y, et al. A Fluorescent Glucose Transport
523 Assay for Screening SGLT2 Inhibitors in Endogenous SGLT2-Expressing HK-2 Cells. Nat Prod
524 Bioprospect. 2019;9(1):13-21.

525 15. Fang P, Yu M, Min W, Wan D, Han S, Shan Y, et al. Effect of baicalin on GLUT4 expression
526 and glucose uptake in myotubes of rats. Life Sciences. 2018;196:156-61.

527 16. Ferreira JM, Burnett AL, Rameau GA. Activity-dependent regulation of surface glucose
528 transporter-3. J Neurosci. 2011;31(6):1991-9.

529 17. Marín-Juez R, Rovira M, Crespo D, van der Vaart M, Spaink HP, Planas JV. GLUT2-
530 mediated glucose uptake and availability are required for embryonic brain development in zebrafish.
531 J Cereb Blood Flow Metab. 2015;35(1):74-85.

532 18. Meireles P, Sales-Dias J, Andrade CM, Mello-Vieira J, Mancio-Silva L, Simas JP, et al.
533 GLUT1-mediated glucose uptake plays a crucial role during Plasmodium hepatic infection. Cell
534 Microbiol. 2017;19(2).

535 19. Blodgett AB, Kothinti RK, Kamyshko I, Petering DH, Kumar S, Tabatabai NM. A
536 fluorescence method for measurement of glucose transport in kidney cells. Diabetes Technol Ther.
537 2011;13(7):743-51.

538 20. Rumin J, Bonnefond H, Saint-Jean B, Rouxel C, Sciandra A, Bernard O, et al. The use of
539 fluorescent Nile red and BODIPY for lipid measurement in microalgae. Biotechnology for Biofuels.
540 2015;8(1):42.

541 21. Bromley SK, Akbaba H, Mani V, Mora-Buch R, Chasse AY, Sama A, et al. CD49a Regulates
542 Cutaneous Resident Memory CD8(+) T Cell Persistence and Response. Cell Rep.
543 2020;32(9):108085.

544 22. Sukumar M, Liu J, Ji Y, Subramanian M, Crompton JG, Yu Z, et al. Inhibiting glycolytic
545 metabolism enhances CD8+ T cell memory and antitumor function. J Clin Invest.
546 2013;123(10):4479-88.

547 23. Jacobs SR, Herman CE, Maciver NJ, Wofford JA, Wieman HL, Hammen JJ, et al. Glucose
548 uptake is limiting in T cell activation and requires CD28-mediated Akt-dependent and independent
549 pathways. J Immunol. 2008;180(7):4476-86.

550 24. Loi S, Sirtaine N, Piette F, Salgado R, Viale G, Van Eenoo F, et al. Prognostic and predictive
551 value of tumor-infiltrating lymphocytes in a phase III randomized adjuvant breast cancer trial in
552 node-positive breast cancer comparing the addition of docetaxel to doxorubicin with doxorubicin-
553 based chemotherapy: BIG 02-98. J Clin Oncol. 2013;31(7):860-7.

554 25. Denkert C, Loibl S, Noske A, Roller M, Muller BM, Komor M, et al. Tumor-associated
555 lymphocytes as an independent predictor of response to neoadjuvant chemotherapy in breast cancer. J
556 Clin Oncol. 2010;28(1):105-13.

557 26. Wang R, Song Y, Hu T, Wang X, Jiang Y, Zhang D, et al. Decreased CD8(+) Lymphocytic
558 Infiltration in Multifocal and Multicentric Glioblastomas. Front Oncol. 2021;11:748277.

559 27. Smazynski J, Webb JR. Resident Memory-Like Tumor-Infiltrating Lymphocytes (TILRM):
560 Latest Players in the Immuno-Oncology Repertoire. Front Immunol. 2018;9:1741.

561

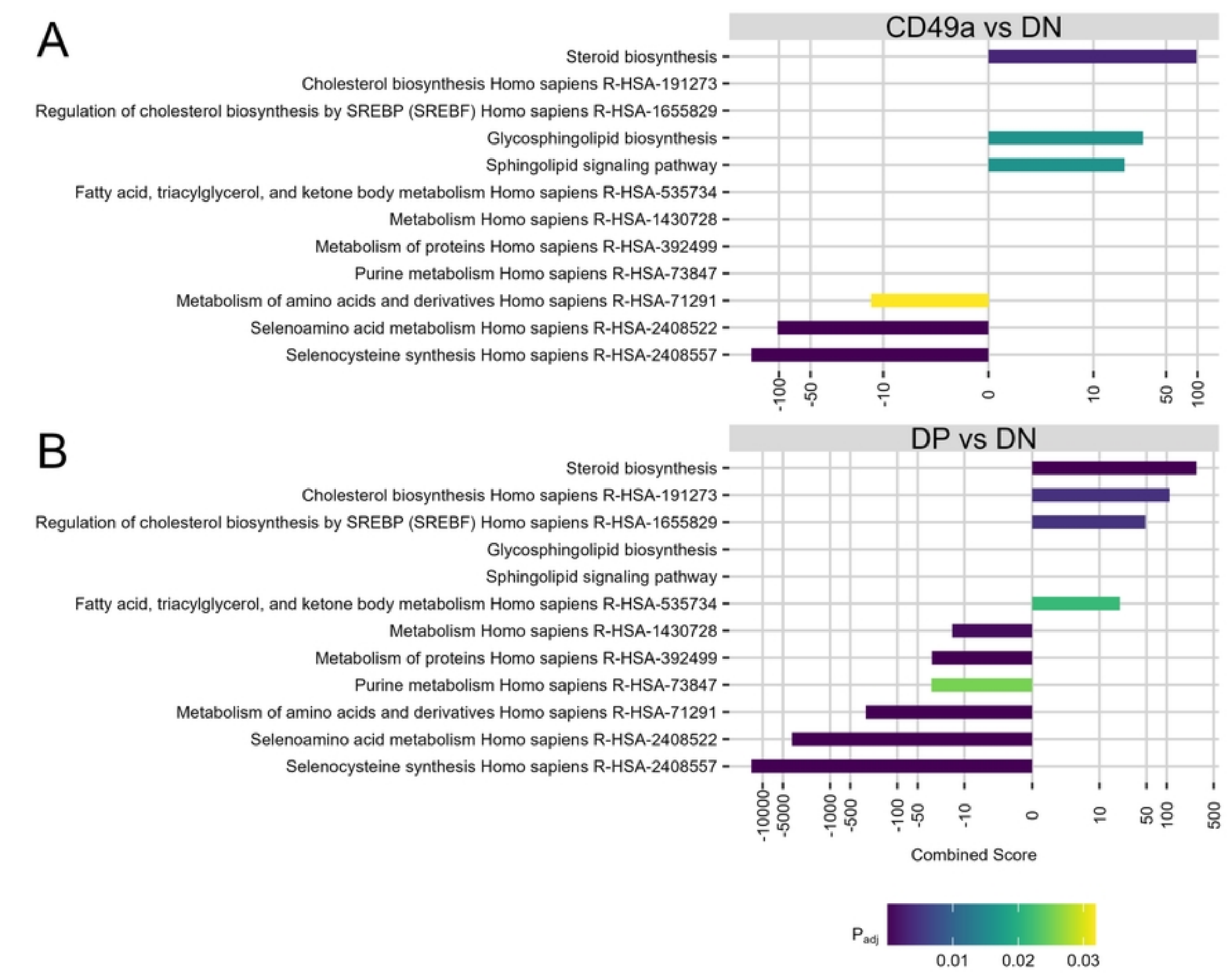
A
CD49a vs DN
Steroid biosynthesis
Cholesterol biosynthesis Homo sapiens R-HSA-191273
Regulation of cholesterol biosynthesis by SREBP (SREBF) Homo sapiens R-HSA-1655829
Glycosphingolipid biosynthesis
Sphingolipid signaling pathway
Fatty acid, triacylglycerol, and ketone body metabolism Homo sapiens R-HSA-535734
Metabolism Homo sapiens R-HSA-1430728
Metabolism of proteins Homo sapiens R-HSA-392499
Purine metabolism Homo sapiens R-HSA-73847
Metabolism of amino acids and derivatives Homo sapiens R-HSA-71291
Selenoamino acid metabolism Homo sapiens R-HSA-2408522
Selenocysteine synthesis Homo sapiens R-HSA-2408557
-100
-50
-10
0
10
50
100
B
DP vs DN
Steroid biosynthesis
Cholesterol biosynthesis Homo sapiens R-HSA-191273
Regulation of cholesterol biosynthesis by SREBP (SREBF) Homo sapiens R-HSA-1655829
Glycosphingolipid biosynthesis
Sphingolipid signaling pathway
Fatty acid, triacylglycerol, and ketone body metabolism Homo sapiens R-HSA-535734
Metabolism Homo sapiens R-HSA-1430728
Metabolism of proteins Homo sapiens R-HSA-392499
Purine metabolism Homo sapiens R-HSA-73847
Metabolism of amino acids and derivatives Homo sapiens R-HSA-71291
Selenoamino acid metabolism Homo sapiens R-HSA-2408522
Selenocysteine synthesis Homo sapiens R-HSA-2408557
-10000
-5000
-1000
-500
-100
-50
-10
0
10
50
100
500
Combined Score
P_{adj}
0.01
0.02
0.03

Figure 1

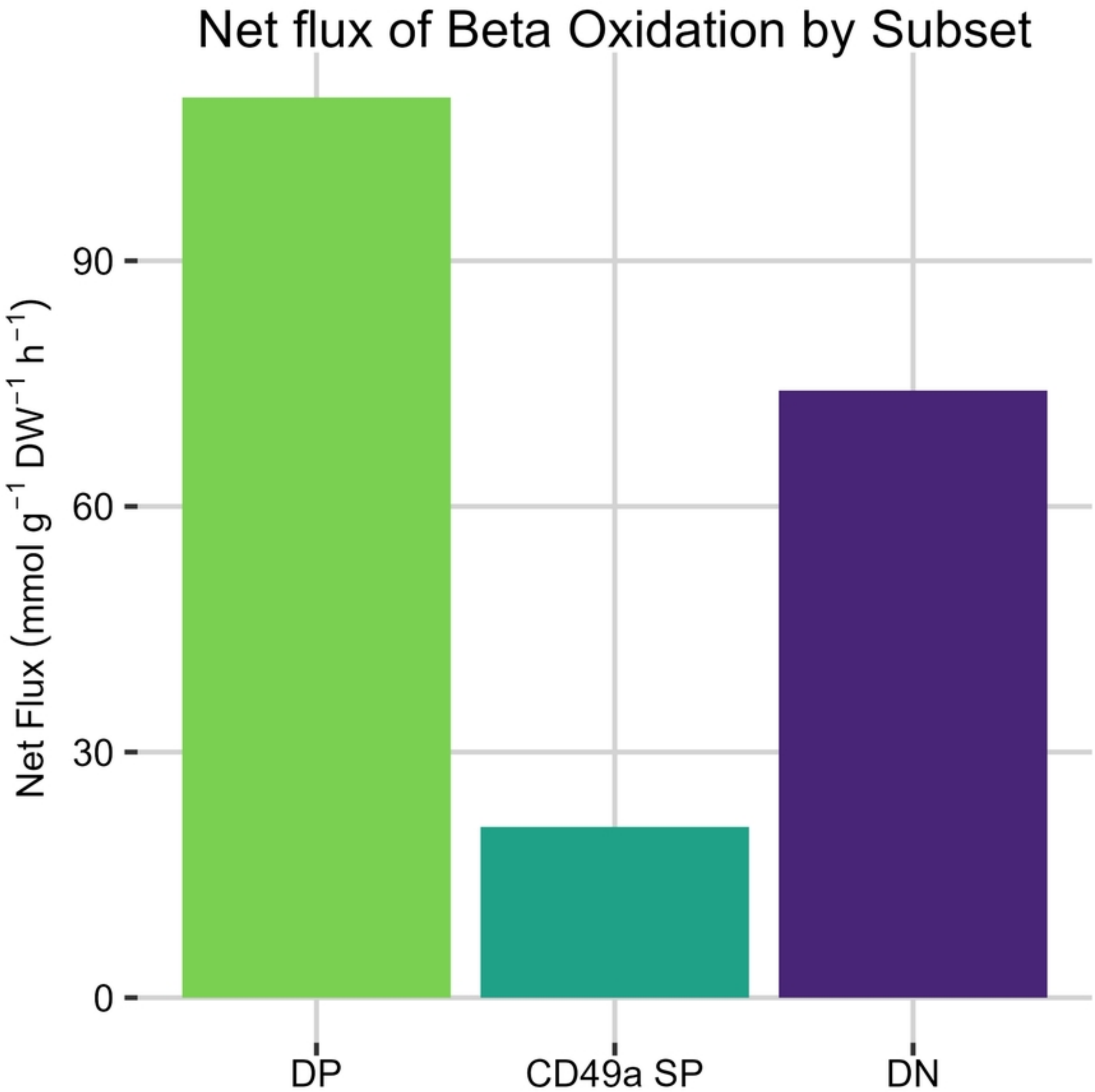
Net flux of Beta Oxidation by Subset
Net Flux (mmol g^{-1} DW^{-1} h^{-1})
90
60
30
0
DP
CD49a SP
DN

Figure 2

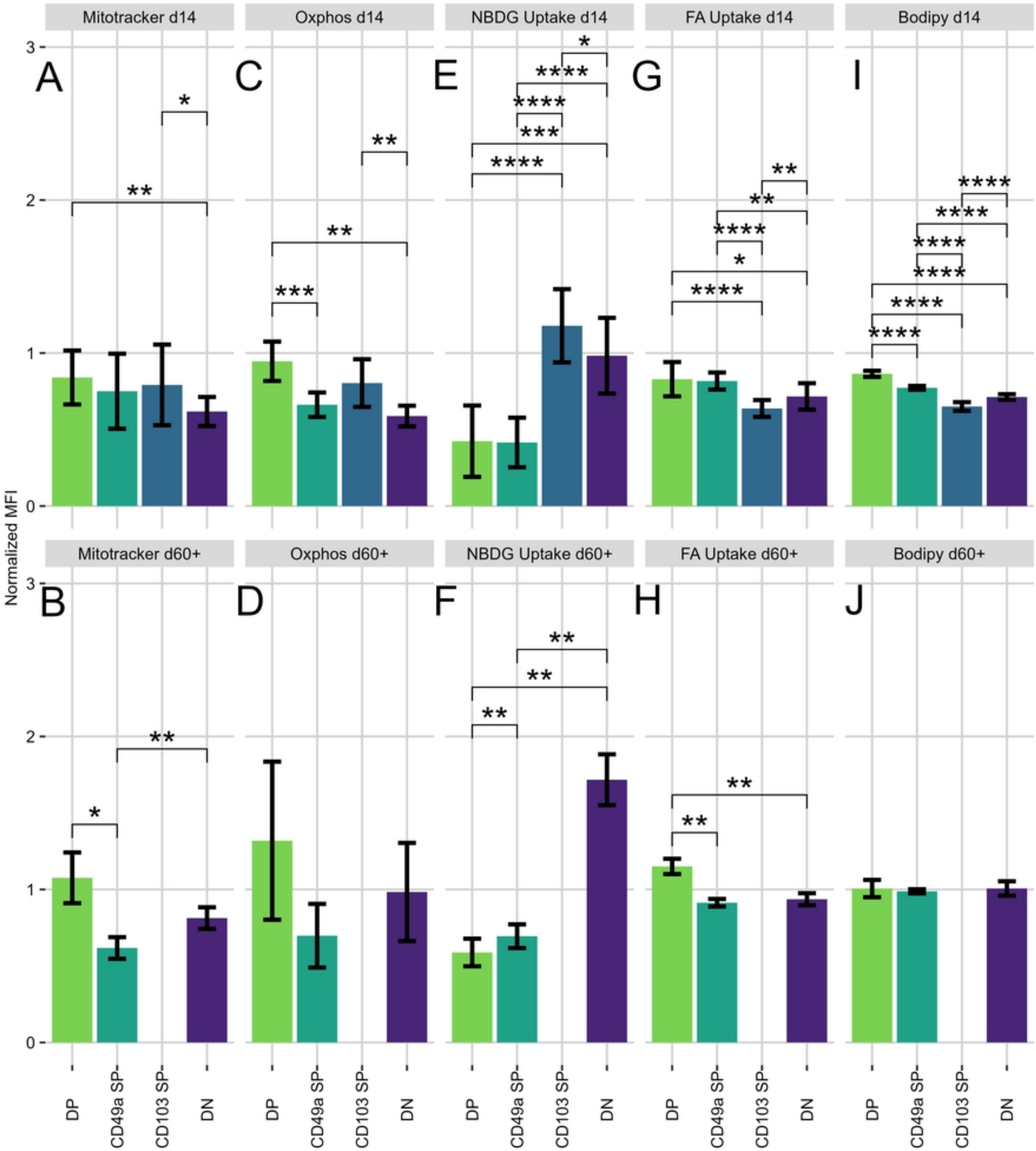
Mitotracker d14
Oxphos d14
NBDG Uptake d14
FA Uptake d14
Bodipy d14
Mitotracker d60+
Oxphos d60+
NBDG Uptake d60+
FA Uptake d60+
Bodipy d60+
A
B
C
D
E
F
G
H
I
J
Normalized MFI
0
1
2
3
DP
CD49a SP-
CD103 SP-
DN

Figure 3

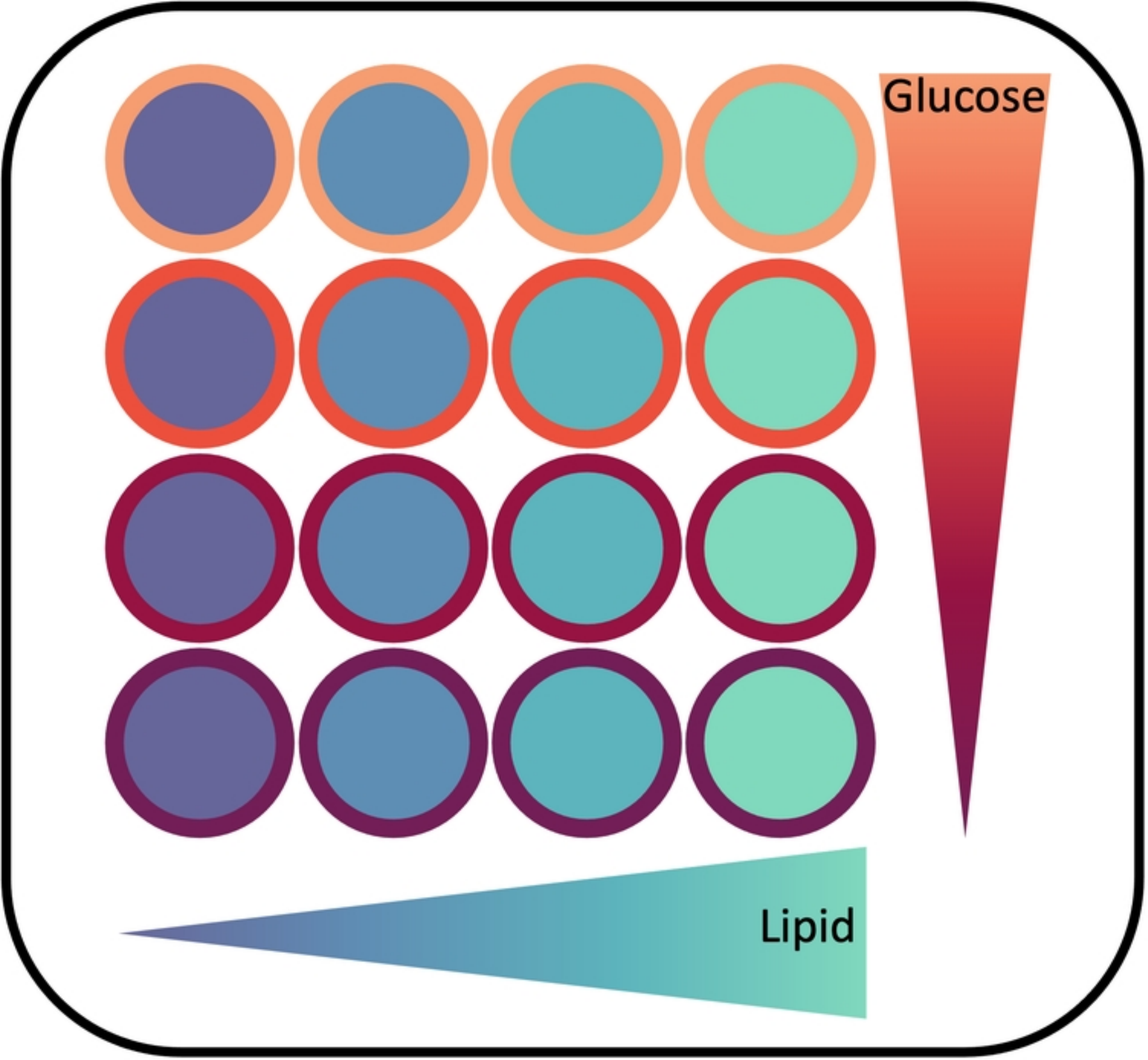

Figure 4

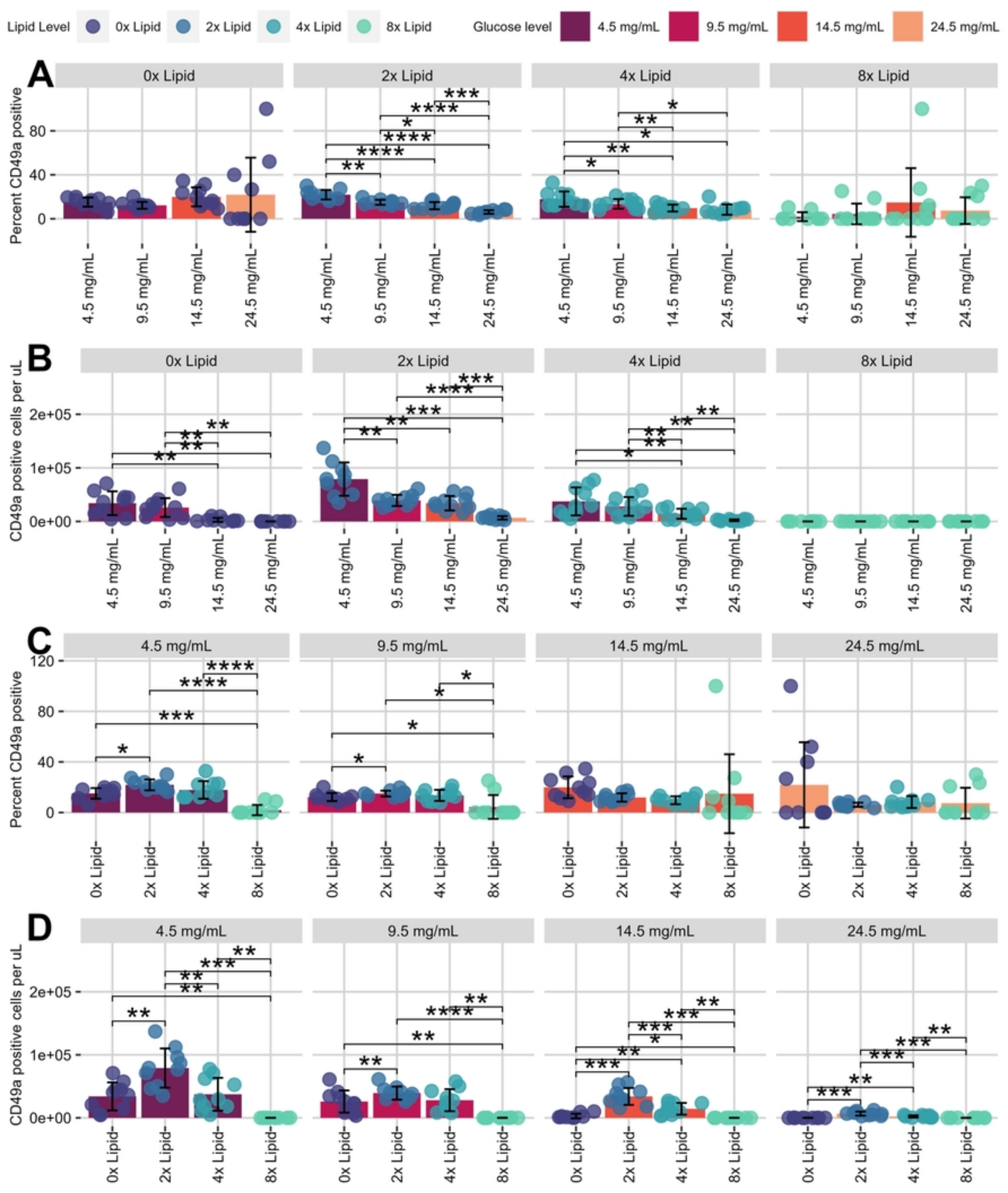
Lipid Level
0x Lipid
2x Lipid
4x Lipid
8x Lipid
Glucose level
4.5 mg/mL
9.5 mg/mL
14.5 mg/mL
24.5 mg/mL
A
Percent CD49a positive
B
CD49a positive cells per uL
C
Percent CD49a positive
D
CD49a positive cells per uL

Figure 5

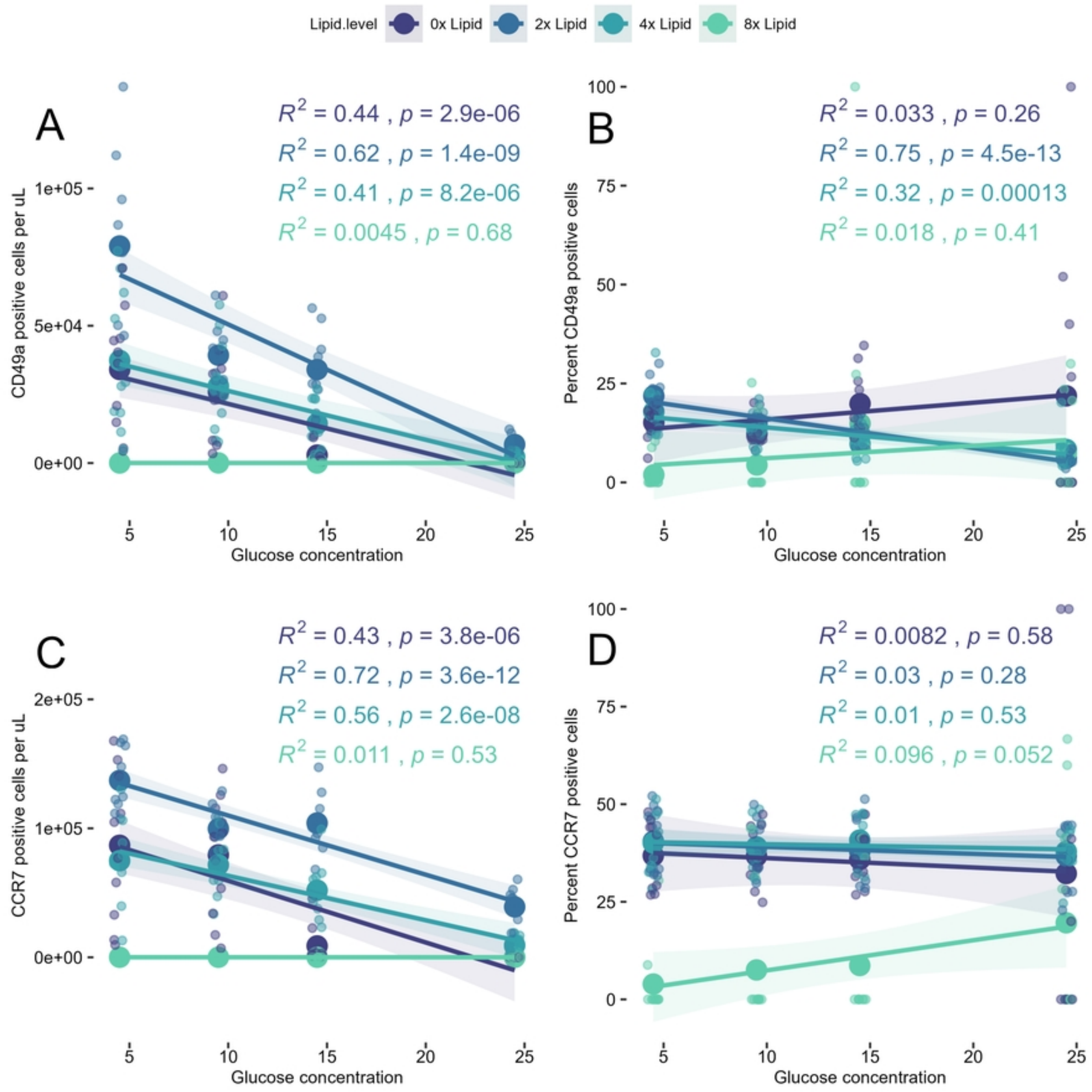
Lipid.level
0x Lipid
2x Lipid
4x Lipid
8x Lipid
A
R^2 = 0.44 , p = 2.9e-06
R^2 = 0.62 , p = 1.4e-09
R^2 = 0.41 , p = 8.2e-06
R^2 = 0.0045 , p = 0.68
CD49a positive cells per uL
1e+05
5e+04
0e+00
5
10
15
20
25
Glucose concentration
B
R^2 = 0.033 , p = 0.26
R^2 = 0.75 , p = 4.5e-13
R^2 = 0.32 , p = 0.00013
R^2 = 0.018 , p = 0.41
Percent CD49a positive cells
100
75
50
25
0
5
10
15
20
25
Glucose concentration
C
R^2 = 0.43 , p = 3.8e-06
R^2 = 0.72 , p = 3.6e-12
R^2 = 0.56 , p = 2.6e-08
R^2 = 0.011 , p = 0.53
CCR7 positive cells per uL
2e+05
1e+05
0e+00
5
10
15
20
25
Glucose concentration
D
R^2 = 0.0082 , p = 0.58
R^2 = 0.03 , p = 0.28
R^2 = 0.01 , p = 0.53
R^2 = 0.096 , p = 0.052
Percent CCR7 positive cells
100
75
50
25
0
5
10
15
20
25
Glucose concentration

Figure 6

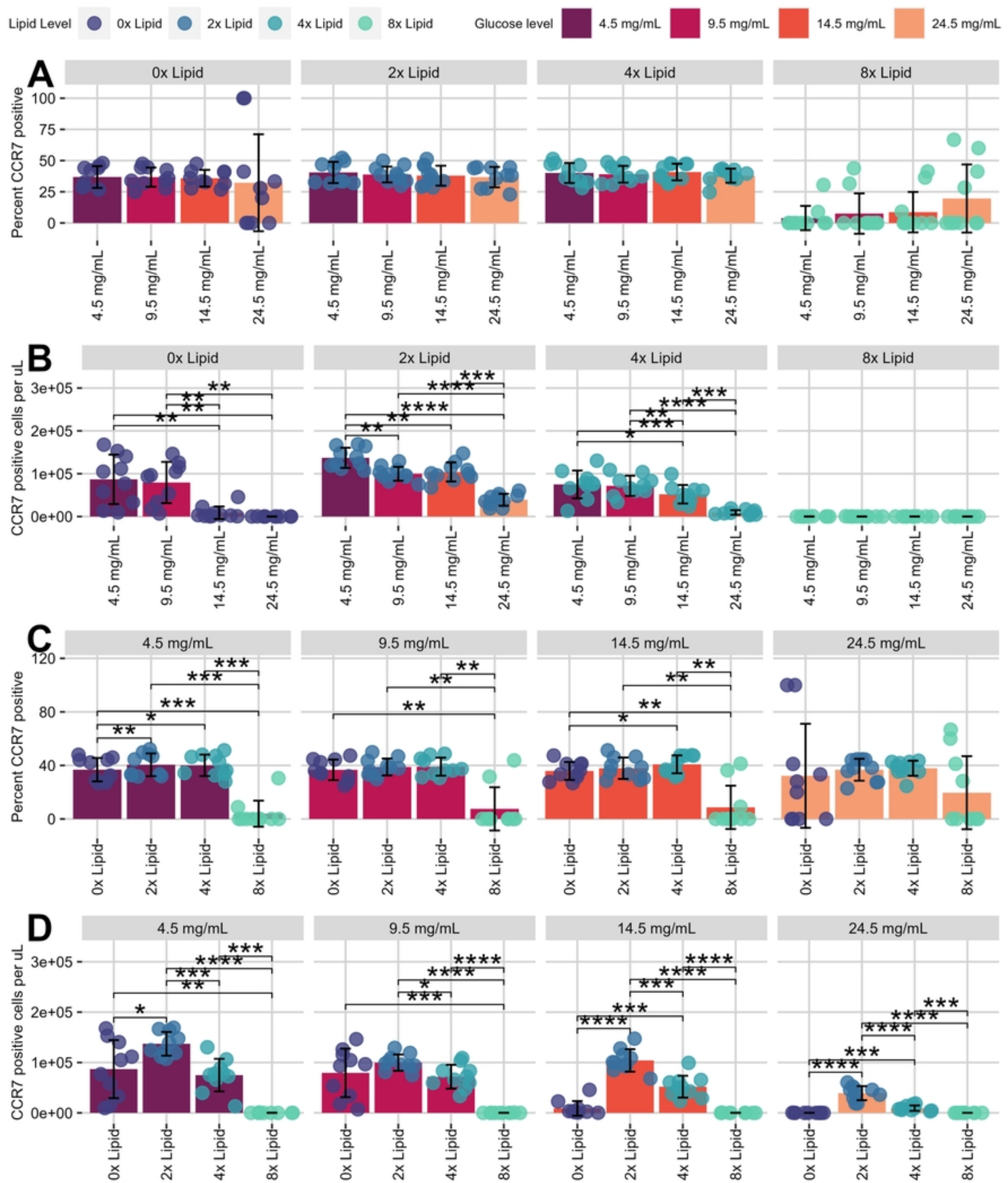
Lipid Level
0x Lipid
2x Lipid
4x Lipid
8x Lipid
Glucose level
4.5 mg/mL
9.5 mg/mL
14.5 mg/mL
24.5 mg/mL
A
Percent CCR7 positive
B
CCR7 positive cells per uL
C
Percent CCR7 positive
D
CCR7 positive cells per uL

Figure 7